



PCCP

**Exploring Mechanistic Routes for Light Alkane Oxidation
with an Iron-Triazolate Metal–Organic Framework**

Journal:	<i>Physical Chemistry Chemical Physics</i>
Manuscript ID	CP-ART-02-2022-000963
Article Type:	Paper
Date Submitted by the Author:	27-Feb-2022
Complete List of Authors:	Rosen, Andrew; Northwestern University, Chemical; Notestein, Justin; Northwestern University, Chemical and Biological Engineering Snurr, Randall; Northwestern University, Department of Chemical & Biological Engineering

SCHOLARONE™
Manuscripts

Exploring Mechanistic Routes for Light Alkane Oxidation with an Iron-Triazolate Metal–Organic Framework

Andrew S. Rosen, Justin M. Notestein,* Randall Q. Snurr*

Department of Chemical and Biological Engineering, Northwestern University, 2145 Sheridan Rd., Evanston, IL 60208 (USA)

*E-mail: j-notestein@northwestern.edu

*E-mail: snurr@northwestern.edu

Abstract. In this work, we computationally explore the formation and subsequent reactivity of various iron-oxo species in the iron–triazolate framework $\text{Fe}_2(\mu\text{-OH})_2(\text{bbta})$ ($\text{H}_2\text{bbta} = 1H,5H\text{-benzo}(1,2\text{-d}:4,5\text{-d}')\text{bistriazole}$) for the catalytic activation of strong C–H bonds. With the direct conversion of methane to methanol as the probe reaction of interest, we use density functional theory (DFT) calculations to evaluate multiple mechanistic pathways in the presence of either N_2O or H_2O_2 oxidants. These calculations reveal that a wide range of transition metal-oxo sites – both terminal and bridging – are plausible in this family of metal–organic frameworks, making it a unique platform for comparing the electronic structure and reactivity of different proposed active site motifs. Based on the DFT calculations, we predict that $\text{Fe}_2(\mu\text{-OH})_2(\text{bbta})$ would exhibit a relatively low barrier for N_2O activation and energetically favorable formation of an $[\text{Fe}(\text{O})]^{2+}$ species that is capable of oxidizing C–H bonds. In contrast, the use of H_2O_2 as the oxidant is predicted to yield an assortment of bridging iron-oxo sites that are less reactive. We also find that abstracting oxo ligands can exhibit a complex mixture of both positive and negative spin density, which may have broader implications for relating the degree of radical character to catalytic activity. In general, we consider the coordinatively unsaturated iron sites to be promising for oxidation catalysis, and we provide several recommendations on how to further tune the catalytic properties of this family of metal–triazolate frameworks.

Introduction

Terminal and bridging transition metal-oxo species are commonly invoked active site motifs in catalytic oxidation reactions, especially those involving the functionalization of C–H bonds.^{1–8} For the purpose of synthetic catalyst design, a judicious selection of metal and ligand environment is needed to yield a metal-oxo species that is thermodynamically and kinetically realizable while being sufficiently reactive towards the substrate of interest. Recently, metal–organic frameworks (MOFs) have proven to be a promising platform to support reactive transition metal-oxo species, as the synthetic tunability of MOFs makes it possible to control the electronic structure environment of the catalytic active sites in a predictable fashion.^{9–12} The well-defined, spatially isolated metals incorporated within the inorganic nodes of MOFs can also enable the isolation of reactive intermediates within a solid-state structure that can oftentimes be challenging to characterize with molecular transition metal-oxo complexes.^{10,13}

Collectively, these factors have led to the design of several MOFs that can support transition metal-oxo species suitable for the catalytic oxidation of strong C–H bonds, such as those of methane and ethane.^{14,15} The first MOFs shown to support high-valent, terminal metal-oxo species that can activate strong C–H bonds were Fe₂(dobdc) (dobdc⁴⁻ = 2,5-dioxido-1,4-benzenedicarboxylate) and its isostructural, Mg-diluted analogue Fe_{0.1}Mg_{1.9}(dobdc),¹⁶ which can convert ethane to ethanol at 75 °C in the presence of N₂O due to the formation of a presumed Fe(IV)-oxo intermediate.^{16–20} Since this pioneering work, several other MOFs have been studied for the selective oxidation of light alkanes via proposed terminal iron-oxo species,^{21–34} such as MIL-100(Fe) (MIL = Materials of Institut Lavoisier) and PCN-250 (PCN = Porous Coordination Network), which were shown to catalytically oxidize methane to methanol in the presence of N₂O at 200 °C and 120 °C, respectively.^{21,35} In addition to terminal iron-oxo species, bridging iron-oxo species have been proposed as crucial catalytic intermediates for the activation of strong C–H bonds using MOF-based catalysts.^{36–40} Perhaps most notably, it was shown that Fe-doped MIL-53(Al) – denoted MIL-53(Al,Fe) – is capable of converting methane to methanol in the presence of H₂O₂ at 60 °C via the formation of a proposed (μ-oxo)diiron(IV) intermediate.^{39,40}

Recently, a highly tunable family of metal–triazolate frameworks with the general formula M₂(μ-Cl)₂(bbta) (M = Mn, Fe, Co, Ni, Cu) (H₂bbta = 1*H*,5*H*-benzo(1,2-*d*:4,5-*d'*)bistriazole) has been synthesized,^{41–45} in addition to a large-pore analogue with the general formula M₂(μ-Cl)₂(btdd) (H₂btdd = bis(1*H*-1,2,3-triazolo[4,5-*b*],[4',5'-*i*])dibenzo[1,4]dioxin).^{42,46} The divalent metal centers in this family of MOFs are known to be coordinatively unsaturated, adopting a square pyramidal coordination geometry suitable for the binding and potential activation of guest molecules, including those that involve oxidation of the metal centers.^{46,47} The structure of these metal–triazolate frameworks closely resembles that of M₂(dobdc), with the main differences being the presence of triazolate functional groups in place of carboxylate functional groups as well as equatorial μ-Cl⁻ ligands in place of O-donor ligands.

When the μ-Cl⁻ ligands of M₂(μ-Cl)₂(bbta) are exchanged with μ-OH⁻ ligands to yield the isostructural framework M₂(μ-OH)₂(bbta) (Figure 1a), the metal centers can become more easily oxidized.^{48–50} As such, it is worth considering if the M₂(μ-OH)₂(bbta) family can support terminal transition metal-oxo species and/or bridging transition metal-oxo species suitable for oxidation catalysis. Several hypothetical transition metal-oxo active site motifs in the M₂(μ-OH)₂(bbta) family are depicted in Figure 1b, each with a different electronic structure environment that may be realized depending on the choice of metal center and oxidant. Aside from its potential use in oxidation catalysis, the diversity of potential active site species also makes M₂(μ-OH)₂(bbta) a unique platform to systematically probe the properties of various transition metal-oxo species that are of broad interest in the (bio)inorganic chemistry community.

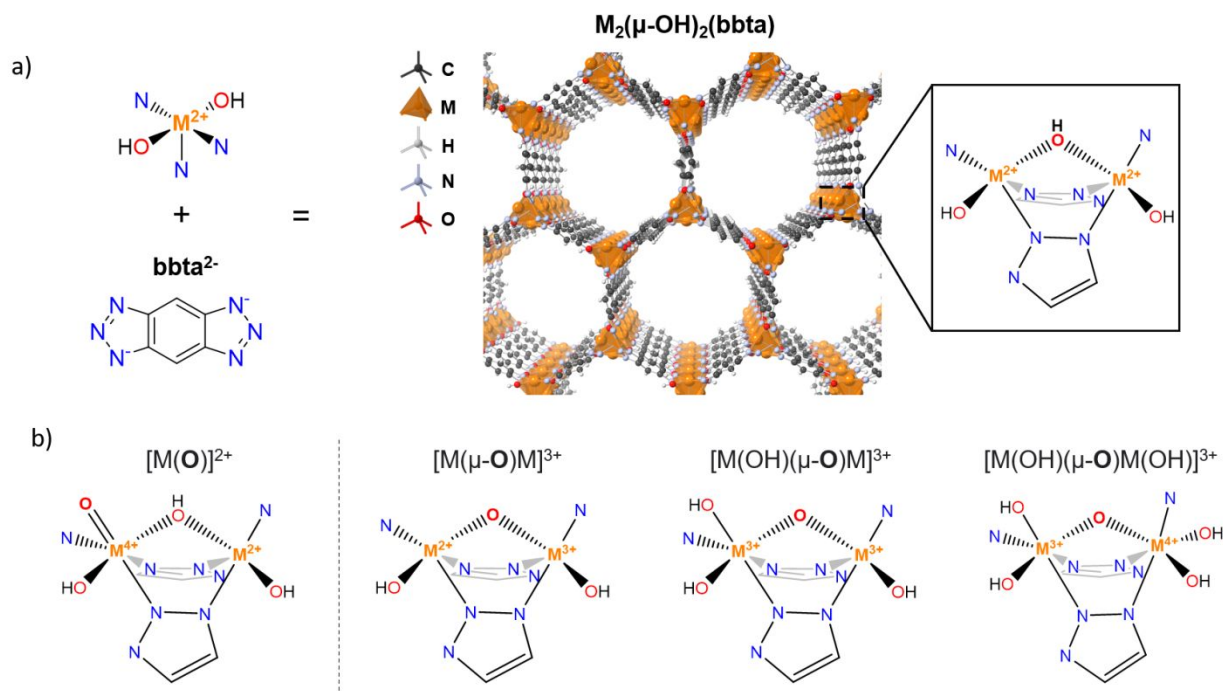


Figure 1. a) Constituent building blocks and periodic structure of $M_2(\mu-OH)_2(bbta)$. Atom color key: M (orange), N (blue), O (red), C (black), H (white). b) Hypothesized terminal and bridging metal-oxo active site motifs that can be considered when $M_2(\mu-OH)_2(bbta)$ is exposed to an oxidant. Only a representative portion of the framework structure is shown. Formal oxidation states are included as a visual aid but do not necessarily reflect the true ground state electron configuration.

In the present study, we use periodic density functional theory (DFT) calculations to investigate the formation and subsequent reactivity of hypothesized terminal and bridging iron-oxo species within $Fe_2(\mu-OH)_2(bbta)$, motivated by the aforementioned work on Fe-containing MOFs. For the reaction of interest, we chose to study the direct conversion of methane to methanol given its societal importance,^{51–53} considering both N_2O and H_2O_2 oxidants as possible ways to produce the intermediates shown in Figure 1. Although $Fe_2(\mu-OH)_2(bbta)$ has not yet been synthesized, its Cl-containing analogue $Fe_2(\mu-Cl)_2(bbta)$ has been reported in the literature.⁴² We note that the isostructural $Co_2(\mu-OH)_2(bbta)$ has been successfully synthesized and studied for a variety of redox processes, including O_2 chemisorption,^{48,50} electrocatalytic oxygen evolution,⁵⁴ and photocatalytic CO_2 reduction.⁵⁵

Based on the results of the DFT calculations, we predict that $Fe_2(\mu-OH)_2(bbta)$ would exhibit particularly promising thermodynamics and kinetics for N_2O activation, resulting in the favorable formation of a terminal iron-oxo species that can activate C–H bonds. When considering H_2O_2 as the oxidant (or other oxidants that can produce $OH\cdot$ radicals), we find that a wider range of iron-oxo species are plausible, including both terminal and bridging iron-oxo sites. An analysis of the electronic structure for each proposed iron-oxo species indicates that spin coupling occurs *en route* to the H-abstraction transition state for each of the investigated iron-oxo species. Additionally, a complex arrangement of both positive and negative spin density is present on the terminal iron-oxo species and at the H-abstraction transition state. We conclude with several hypotheses for how to maximize the catalytic activity in this family of metal-triazolate frameworks based on the insights gained from the mechanistic analyses in this work.

Methods

Density Functional Theory Parameters

Plane-wave DFT calculations were carried out using the Vienna *ab initio* Simulation Package (VASP) v.5.4.4.^{56,57} We elected to use periodic DFT in this work over cluster models⁵⁸ to avoid the limitations of finite-size effects, particularly when considering bridging oxo species that lead to structural distortion across multiple Fe sites and reaction steps that involve traversal of the pore environment. Structure relaxations and energy calculations were carried out at the PBE-D3(BJ) level of theory^{59–61} with an effective Hubbard U correction⁶² of 4.0 eV for the Fe 3d sites (unless otherwise stated). This U value was selected because it accurately reproduces the formation energies of iron oxides⁶³ and has been successfully employed in prior work on iron-containing MOFs.^{49,64,65} In general, the use of a $+U$ correction has been shown to greatly improve upon PBE (with $U = 0$ eV) for oxidation processes in MOFs with coordinatively unsaturated metal sites and reduces the tendency of PBE to artificially destabilize high spin states.⁴⁹ We also anticipate that the use of a $+U$ correction will help reduce the self-interaction error⁶⁶ present in generalized gradient approximation (GGA) functionals that can result in a qualitatively incorrect description of the H-abstraction process when left untreated.²⁰

For the guest-free structures, the lattice constants and atomic positions were simultaneously optimized at the PBE-D3(BJ)+ U level of theory, after which the lattice constants were kept fixed for the remainder of the work. The DFT-optimized lattice constants for the $\text{Fe}_2(\mu\text{-OH})_2(\text{bbta})$ framework are shown in Table S1. For the structurally related $\text{Fe}_2(\mu\text{-Cl})_2(\text{bbta})$ framework, the DFT-computed lattice constants are within 0.7% error of the experimentally reported values (Table S2). For calculations at other levels of theory, the PBE-D3(BJ)+ U lattice constants were employed as a matter of consistency.

A plane-wave kinetic energy cutoff of 520 eV and Γ -centered Monkhorst-Pack⁶⁷ $3 \times 2 \times 2$ k -point grid were used throughout this work unless otherwise stated. The net force on all atoms was converged to within 0.03 eV/Å during all structure relaxations. Gaussian smearing of the band occupancies was applied with a smearing width of 0.01 eV and extrapolation back to the 0 K limit. The accurate precision keyword was enabled in VASP, and symmetry constraints were disabled. The energy within each self-consistent field (SCF) loop was converged to within 10^{-6} eV or tighter. For the GGA+ U (and hybrid GGA) calculations, aspherical contributions inside the projector-augmented wave spheres were included. Various spin states were considered for each structure, and the electron configurations shown in Table S3 were adopted. As done in prior work for this family of materials^{47,48} and several studies on other iron-containing MOFs,^{27–29,40} we invoke ferromagnetic coupling between the metal centers as a matter of computational simplicity and to permit the use of a primitive unit cell, which has an odd number of metal centers along a given chain.

Transition states were identified using a combination of the climbing image nudged elastic band (NEB)⁶⁹ and dimer methods⁷⁰ as implemented in VTST Tools v.179.⁷¹ Partial atomic charges were calculated with the Charge Model 5 (CM5) method⁷² using the Chargemol 09-26-2017⁷³ code, and atomic spin densities were computed with the Bader method using the bader 1.0.3 code from the Henkelman group.⁷⁴ VASPKIT 1.2.5⁷⁵ and VESTA 3.5.7⁷⁶ were used to visualize the spin density. Additional computational details can be found in the Supporting Information.

Comparing GGA, GGA+ U , and Hybrid Calculations

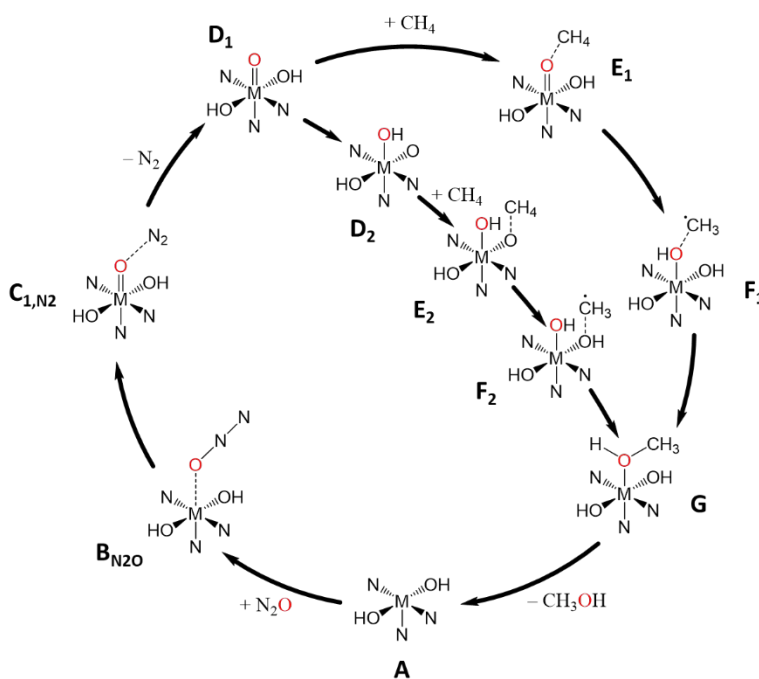
Given the diverse range of active sites and reactions considered in this work, we acknowledge that no single U value is likely to be ideal for each step in the proposed catalytic mechanisms.⁷⁷ As such, we refer the reader to the Supporting Information for a detailed discussion regarding the effect of different density

functional approximations, which includes calculations at the PBE-D3(BJ) (i.e. $U = 0$ eV) and HSE06-D3(BJ)//PBE-D3(BJ)+ U^{78-80} levels of theory for comparison purposes. To briefly summarize, compared to the uncorrected PBE-D3(BJ) functional, we find that the inclusion of a + U correction increases the spin density localized on the metals (Table S9), decreases the spin density localized on the oxo ligand (Table S9), makes the iron-oxo formation energies significantly less exothermic (Tables S10 and S11), increases the barriers for N_2O and H_2O_2 activation (Table S12), and decreases the methane activation barrier (Table S13). Many of these findings are analogous to trends that have been observed when comparing GGAs with hybrid functionals^{18,20,81} and the general observation that there is often a tradeoff between active site stability and reactivity for MOFs.²⁴ In most cases, the single-point HSE06-D3(BJ) calculations do not substantially alter the results of the PBE-D3(BJ)+ U level of theory (Figures S6–S8); notable differences are discussed throughout the text.

Results and Discussion

C–H Bond Activation with an N_2O Oxidant

A proposed mechanism for the direct conversion of methane to methanol in the presence of an N_2O oxidant is shown in Scheme 1. The outer pathway is a commonly proposed terminal metal-oxo route, wherein cleavage of the N–O bond of N_2O results in the formation of an $[M(O)]^{2+}$ species and N_2 (C_{1,N_2}). If the terminal metal-oxo species (D_1) is successfully formed, it can potentially be followed by methane adsorption (E_1), cleavage of the C–H bond of methane (F_1), subsequent rebound of the resulting methyl radical to form methanol (G), and desorption of the methanol product to close the catalytic cycle. The proposed inner pathway is specific to the $M_2(\mu-OH)_2$ (bbta) family of materials and represents an internal H-transfer from a $\mu-OH^-$ species to the proposed terminal oxo moiety. If this step is thermodynamically and kinetically feasible, then a bridging oxo species (D_2), $[M(OH)(\mu-O)M]^{3+}$, may form. Following the adsorption of methane (E_2), H-abstraction may then occur over the bridging oxo species (F_2). The resulting methyl radical can then interact with the terminal hydroxide ligand to generate methanol (G) and complete the catalytic transformation.



Scheme 1. Proposed mechanistic pathways for the conversion of methane to methanol using N_2O as the oxidant and an $\text{M}_2(\mu\text{-OH})_2(\text{bbta})$ catalyst.

When investigating N_2O as a potential oxidant, the first aspect that must be considered is whether N_2O preferentially adsorbs in an $\eta^1\text{-N}$ or $\eta^1\text{-O}$ mode (Figure S2), the latter of which is the preferred configuration for the formation of a terminal metal-oxo site. For $\text{Fe}_2(\mu\text{-OH})_2(\text{bbta})$, the $\eta^1\text{-N}$ and $\eta^1\text{-O}$ geometries are within 2 kJ/mol (Table S4), suggesting that a mixture of both adsorption modes would likely be observed experimentally (similar to $\text{Fe}_{0.1}\text{Mg}_{1.9}(\text{dobdc})$ ¹⁶). For the $\eta^1\text{-O}$ mode, N_2O adsorption in $\text{Fe}_2(\mu\text{-OH})_2(\text{bbta})$ is predicted to take place with an adsorption energy ($\text{A} + \text{N}_2\text{O} \rightarrow \text{B}_{\text{N}_2\text{O}}$) of approximately -22 kJ/mol, consistent with physisorption (Figure 2a).

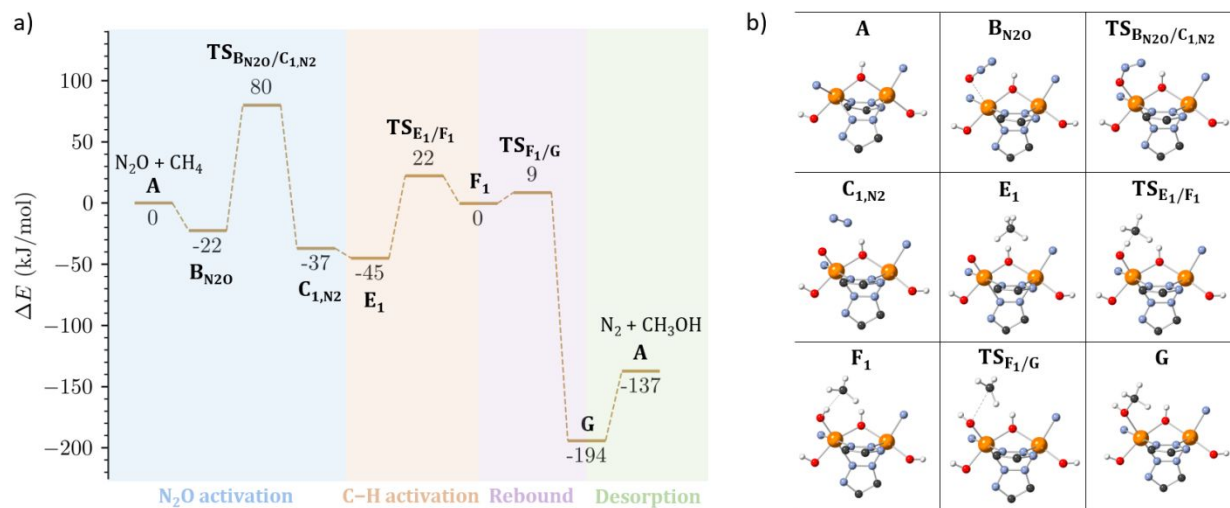


Figure 2. a) Potential energy landscape for the conversion of methane to methanol via a terminal iron-oxo species formed in the presence of an N_2O oxidant and an $\text{Fe}_2(\mu\text{-OH})_2(\text{bbta})$ catalyst. The zero-energy reference corresponds to the infinitely separated reactants (i.e. $\text{A} + \text{N}_2\text{O} + \text{CH}_4$). Results are presented at the PBE-D3(BJ)+ U level of theory. b) Representative portions of the DFT-optimized structures considered in the proposed mechanism. Atom color key: Fe (orange), N (blue), O (red), C (black), H (white).

Following N_2O adsorption in the $\eta^1\text{-O}$ mode ($\text{B}_{\text{N}_2\text{O}}$), cleavage of the N–O bond may occur to yield a formally Fe(IV)-oxo species and the release of N_2 (C_{1,N_2}). The transition state for this process ($\text{TS}_{\text{B}_{\text{N}_2\text{O}}/\text{C}_{1,\text{N}_2}}$) is characterized by a decrease in the Fe–ON₂ distance, stretching of the N–O bond, and reduction of the otherwise linear N–O–O bond angle as the N_2O molecule begins to dissociate (Table S5). As shown in Figure 2a, the barrier for N_2O activation with $\text{Fe}_2(\mu\text{-OH})_2(\text{bbta})$ is predicted to be 102 kJ/mol at the PBE-D3(BJ)+ U level of theory, which is 27 kJ/mol lower than that of $\text{Fe}_2(\text{dobdc})$ at the same level of theory (Table S6), suggesting that this metal–triazolate framework may be able to activate N_2O since $\text{Fe}_2(\text{dobdc})$ can do so at 75 °C. Additionally, the presence of $\mu\text{-OH}^-$ ligands as opposed to $\mu\text{-Cl}^-$ ligands reduces the N_2O activation barrier by 41 kJ/mol (Table S6), which further supports the decision to focus on $\text{M}_2(\mu\text{-OH})_2(\text{bbta})$ for catalytic oxidation reactions.

$\text{Fe}_2(\mu\text{-OH})_2(\text{bbta})$ exhibits an energetically favorable formation of the $[\text{Fe}(\text{O})]^{2+}$ species with a net reaction energy ($\text{B}_{\text{N}_2\text{O}} \rightarrow \text{C}_{1,\text{N}_2}$) of -15 kJ/mol at the PBE-D3(BJ)+ U level of theory, as shown in Figure 2a. When comparing the $[\text{Fe}(\text{O})]^{2+}$ site of $\text{Fe}_2(\mu\text{-OH})_2(\text{bbta})$ to that of $\text{Fe}_2(\text{dobdc})$ at the same level of theory, we find that the reaction energy associated with forming the $[\text{Fe}(\text{O})]^{2+}$ site is 32 kJ/mol more favorable for $\text{Fe}_2(\mu\text{-OH})_2(\text{bbta})$ (Table S7), and both frameworks have the same Fe–O bond distance of 1.65 Å. The greater thermodynamic stability of the $[\text{Fe}(\text{O})]^{2+}$ site in $\text{Fe}_2(\mu\text{-OH})_2(\text{bbta})$ suggests that, if formed, this

active site motif may have a longer lifetime than an analogous $[\text{Fe}(\text{O})]^{2+}$ site in $\text{Fe}_2(\text{dobdc})$, which has been invoked^{16,17} but never directly observed.

Shifting focus to the C–H activation step, we find that proposed $[\text{Fe}(\text{O})]^{2+}$ sites in $\text{Fe}_2(\mu\text{-OH})_2(\text{bbta})$ exhibit a methane activation barrier ($\mathbf{E}_1 \rightarrow \mathbf{TS}_{\mathbf{E}_1/\mathbf{F}_1}$) of 67 kJ/mol at the PBE-D3(BJ)+ U level of theory (Figure 2a). As a point of comparison, the methane activation barrier over $[\text{Fe}(\text{O})]^{2+}$ sites in $\text{Fe}_2(\text{dobdc})$, which is known to catalytically oxidize various alkanes (e.g. ethane,¹⁶ cyclohexane⁸²), is 44 kJ/mol at the same level of theory (Table S8). This finding suggests that the hypothesized $[\text{Fe}(\text{O})]^{2+}$ sites of $\text{Fe}_2(\mu\text{-OH})_2(\text{bbta})$ may be able to activate strong C–H bonds, although the $[\text{Fe}(\text{O})]^{2+}$ sites of $\text{Fe}_2(\text{dobdc})$ are likely to be more reactive. Rebound of the methyl radical to yield methanol ($\mathbf{F}_1 \rightarrow \mathbf{TS}_{\mathbf{F}_1/\mathbf{G}}$) proceeds with a kinetic barrier of only 9 kJ/mol, followed by a methanol desorption energy ($\mathbf{G} \rightarrow \mathbf{A} + \text{CH}_3\text{OH}$) of 57 kJ/mol. Based on these results, we predict that the N_2O activation step will have the largest barrier in the proposed mechanism for converting methane to methanol via a terminal iron-oxo intermediate, as has been predicted for other iron MOFs that are known to oxidize light alkanes.^{17,22,28}

We also explored the possibility of an internal H-transfer from the bridging $\mu\text{-OH}^-$ species to the terminal oxo ligand ($\mathbf{D}_1 \rightarrow \mathbf{D}_2$ in Scheme 1). For $\text{Fe}_2(\mu\text{-OH})_2(\text{bbta})$, the $[\text{Fe}(\text{OH})(\mu\text{-O})\text{Fe}]^{3+}$ species (\mathbf{D}_2) is predicted to be 18 kJ/mol more energetically favorable than the $[\text{Fe}(\text{O})]^{2+}$ (\mathbf{D}_1) species at the PBE-D3(BJ)+ U level of theory (Figure 3). However, there is a relatively large kinetic barrier of 92 kJ/mol for the internal H-transfer process to take place. Given the lower barrier for C–H activation, the $[\text{Fe}(\text{O})]^{2+}$ species — if formed — may predominantly react with the substrate of interest rather than form a bridging iron-oxo species. Nonetheless, the presence of bridging iron-oxo species cannot be entirely excluded, especially in the absence of methane or other hydrocarbon reactants.

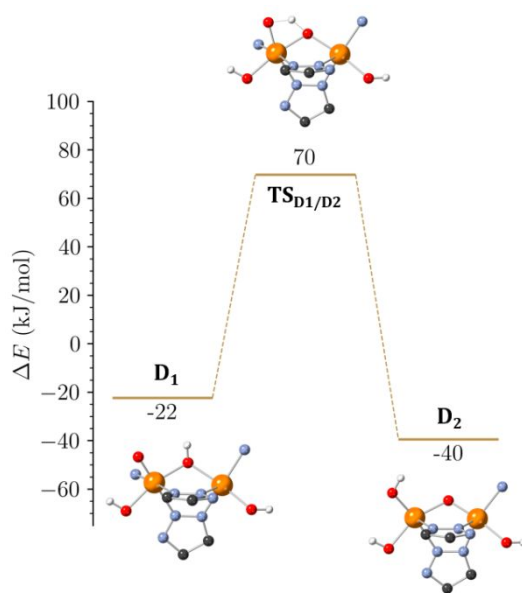
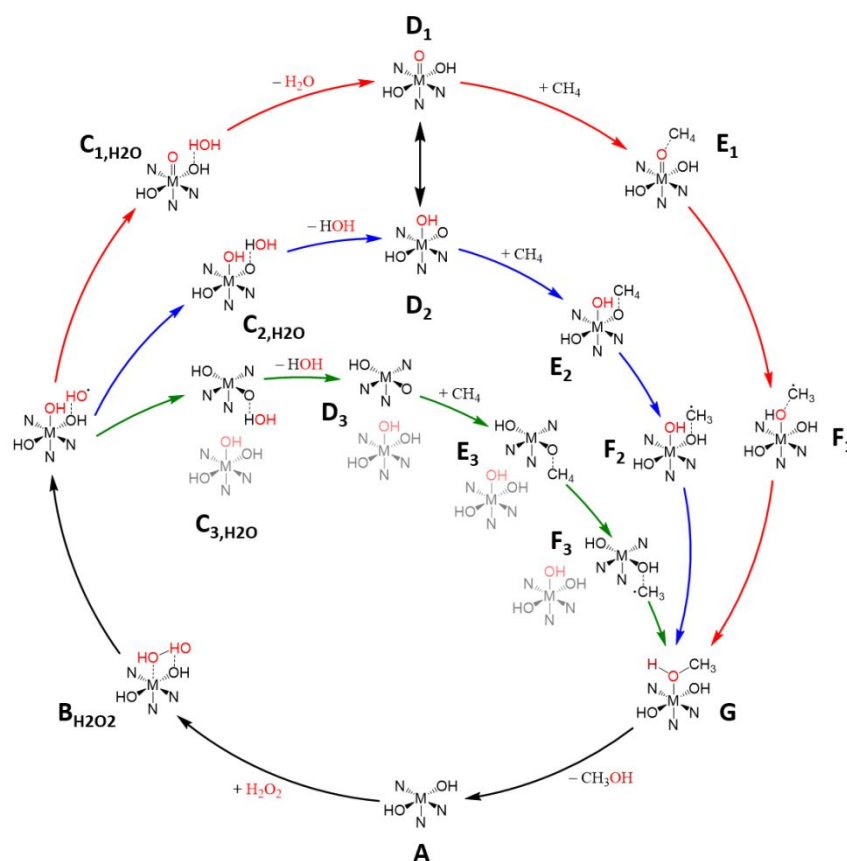


Figure 3. Potential energy landscape and corresponding DFT-optimized structures for an internal H-transfer process from the $\mu\text{-OH}^-$ group to the terminal oxo species of $\text{Fe}_2(\mu\text{-OH})_2(\text{bbta})$. The zero-energy reference corresponds to the infinitely separated reactants (i.e. $\mathbf{A} + \text{N}_2\text{O} + \text{CH}_4$). Results are presented at the PBE-D3(BJ)+ U level of theory. Representative portions of the DFT-optimized structures considered in the proposed mechanism are shown. Atom color key: Fe (orange), N (blue), O (red), C (black), H (white).

C–H Bond Activation with an H₂O₂ Oxidant

Recognizing that the $\mu\text{-OH}^-$ species in the $\text{M}_2(\mu\text{-OH})_2(\text{bbta})$ framework may react with $\text{OH}\cdot$ radicals, we also considered methane activation in the presence of an H_2O_2 oxidant via several proposed mechanisms, as summarized in Scheme 2. All the mechanisms shown in Scheme 2 begin with H_2O_2 adsorbing at a coordinatively unsaturated metal site ($\text{B}_{\text{H}_2\text{O}_2}$). Provided the barrier is sufficiently low, H_2O_2 activation may occur to yield a terminal $\text{M}\text{-OH}$ site and nearby $\text{OH}\cdot$ radical. Given the reactive nature of the $\text{OH}\cdot$ radical, multiple pathways were considered based on which species it interacts with. The outermost (red) route is analogous to the $[\text{M}(\text{O})]^{2+}$ (D_1) route of the N_2O activation mechanism (Scheme 1); in this pathway, the $\text{OH}\cdot$ radical abstracts an H atom from the terminal hydroxide ligand to yield a terminal metal-oxo site and H_2O ($\text{C}_{1,\text{H}_2\text{O}}$) before activating the C–H bond of methane ($\text{E}_1 \rightarrow \text{F}_1$). The central (blue) pathway is analogous to the $[\text{M}(\text{OH})(\mu\text{-O})\text{M}]^{3+}$ (D_2) route of the N_2O activation mechanism (Scheme 1); in this pathway, the $\text{OH}\cdot$ radical abstracts an H atom from the $\mu\text{-OH}^-$ species to form a bridging metal-oxo site and H_2O ($\text{C}_{2,\text{H}_2\text{O}}$), and the bridging metal-oxo activates the C–H bond of methane ($\text{E}_2 \rightarrow \text{F}_2$). Finally, in the innermost (green) pathway, a terminal OH ligand and bridging oxo species are formed along two adjacent – but distinct – chains of metal centers within the framework following H_2O_2 activation, yielding separate $[\text{M}(\mu\text{-O})\text{M}]^{3+}$ and $[\text{M}\text{-OH}]^{2+}$ sites (D_3), the former of which is considered for C–H activation in this work ($\text{E}_3 \rightarrow \text{F}_3$). In all cases, the methyl radical can form methanol ($\text{F}_i \rightarrow \text{G}$) and desorb to regenerate the starting material.



Scheme 2. Proposed mechanistic pathways for the conversion of methane to methanol using H_2O_2 as the oxidant and an $\text{M}_2(\mu\text{-OH})_2(\text{bbta})$ catalyst. In the outermost red pathway, a terminal metal-oxo species is formed with possible internal H-transfer to yield a bridging oxo species ($\text{D}_1 \rightarrow \text{D}_2$). In the middle blue pathway, a terminal OH ligand and bridging oxo species are formed around the same metal center. In the innermost green pathway, a terminal OH ligand and bridging oxo species are formed along two adjacent but distinct chains of metal centers within the framework.

Beginning with the H_2O_2 adsorption step ($\text{A} + \text{H}_2\text{O}_2 \rightarrow \text{B}_{\text{H}_2\text{O}_2}$), we predict that $\text{Fe}_2(\mu\text{-OH})_2(\text{bbta})$ exhibits strong chemisorption of H_2O_2 with an adsorption energy of -81 kJ/mol (Figure 4). In this framework, H-bonding interactions between the $\mu\text{-OH}^-$ ligands and H_2O_2 contribute to the highly favorable adsorption process (similar to how $\text{Co}_2(\mu\text{-OH})_2(\text{bbta})$ exhibits H-bonding interactions with O_2 adsorbates^{48,50}). Following H_2O_2 adsorption, we predict relatively low H_2O_2 activation barriers ($\text{B}_{\text{H}_2\text{O}_2} \rightarrow \text{C}_{1,\text{H}_2\text{O}}/\text{C}_{2,\text{H}_2\text{O}}/\text{C}_{3,\text{H}_2\text{O}}$) of $45 - 62$ kJ/mol at the PBE-D3(BJ)+ U level of theory depending on the pathway under investigation (Figure 4). These barriers are associated with the cleavage of the O–O bond in H_2O_2 , which results in the formation of a transient $\text{OH}\cdot$ species and Fe–OH group before forming the $\text{C}_{\text{H}_2\text{O}}$ products. We note that in prior experimental work, it has been shown that both $\text{Mn}_2\text{Cl}_2(\text{bbta})$ and $\text{Co}_2\text{Cl}_2(\text{bbta})$ can be oxidized in the presence of H_2O_2 at 0°C ,⁴³ although these frameworks do not have $\mu\text{-OH}^-$ ligands that may interact with $\text{OH}\cdot$ species from H_2O_2 .

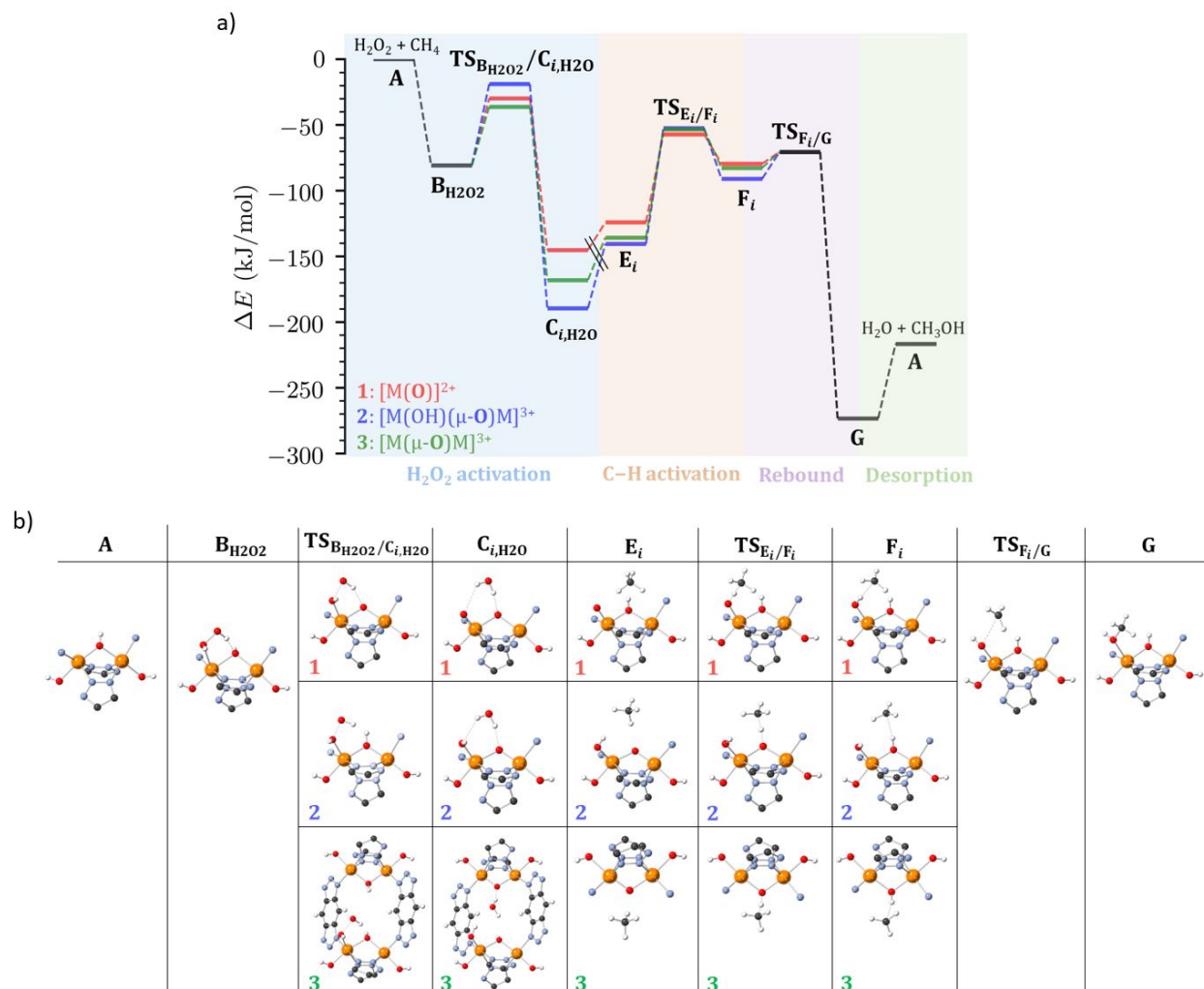


Figure 4. a) Potential energy landscape for the conversion of methane to methanol in the presence of an H_2O_2 oxidant and $\text{Fe}_2(\mu\text{-OH})_2(\text{bbta})$ catalyst. The zero-energy reference corresponds to the infinitely separated reactants (i.e. $\text{A} + \text{H}_2\text{O}_2 + \text{CH}_4$). Results are presented at the PBE-D3(BJ)+ U level of theory. Color key: $[\text{Fe}(\text{O})]^{2+}$ (red), $[\text{Fe}(\text{OH})(\mu\text{-O})\text{Fe}]^{3+}$ (blue), and $[\text{Fe}(\mu\text{-O})\text{Fe}]^{3+}$ (green) pathways. b) Representative portions of the DFT-optimized intermediates and transition states associated with $\text{Fe}_2(\mu\text{-OH})_2(\text{bbta})$. Atom color key: Fe (orange), N (blue), O (red), C (black), H (white).

As shown in Figure 4, at the PBE-D3(BJ)+*U* level of theory the $[\text{Fe}(\text{O})]^{2+}$ site (\mathbf{E}_1) is predicted to be more reactive towards C–H bonds than the bridging iron-oxo species invoked in Scheme 2 ($\mathbf{E}_2/\mathbf{E}_3$). The higher reactivity of the $[\text{Fe}(\text{O})]^{2+}$ site can likely be rationalized based on the higher formal oxidation state of the Fe site compared to that in the bridging iron-oxo species. Nonetheless, all three iron-oxo species have methane activation barriers below 100 kJ/mol at the PBE-D3(BJ)+*U* level of theory (Figure 4), suggesting that even the bridging oxo motifs may exhibit some degree of reactivity towards substrates with weaker C–H bonds (even if they may not be able to activate methane in practice). While it is the most reactive of the oxo ligands investigated in this work, the terminal iron-oxo species is also the least energetically preferred when considering H_2O_2 as the oxidant. In addition to the radical methane dissociation pathways shown in Figure 4, we also considered surface-stabilized methane dissociation⁸³ at the \mathbf{D}_2 site (Figure S5); however, the surface-stabilized route was found to have a 15 kJ/mol larger C–H activation barrier at the PBE-D3(BJ)+*U* level of theory.

Following the C–H activation step, rebound of the methyl radical occurs with the smallest barrier throughout the proposed mechanism, consistent with most prior studies.¹⁴ In contrast with the N_2O mechanism where cleaving the N–O bond has the largest activation energy (Figure 2), C–H activation is more likely to be the step with the largest barrier when using H_2O_2 as the oxidant, especially if bridging iron-oxo sites are the sole or predominant active site species. In general, the HSE06-D3(BJ)//PBE-D3(BJ)+*U* calculations for the H_2O_2 -based mechanism (Figure S8) yield analogous trends, but the bridging iron-oxo species are predicted to be even more energetically favorable (with a larger C–H activation barrier as a result). Based on these calculations, H_2O_2 should only be considered if bridging iron-oxo species are known to be desirable for a given oxidation reaction of interest, although such sites are less reactive than proposed $[\text{Fe}(\text{O})]^{2+}$ species that may be realized with other oxidants.

Electronic Structure of Various Iron-Oxo Species

From the prior analyses, we can conclude that there are several plausible metal-oxo species that should be considered for catalytic oxidation reactions with the $\text{M}_2(\mu\text{-OH})_2(\text{bbta})$ family of materials. In this section, we explore the electronic structure of the metal-oxo sites outlined in Figure 1b. Specifically, we consider the terminal iron-oxo site, $[\text{Fe}(\text{O})]^{2+}$, which can be formally described as an Fe(IV)-oxo species, as well as three related bridging iron-oxo sites: $[\text{Fe}(\mu\text{-O})\text{Fe}]^{3+}$, $[\text{Fe}(\text{OH})(\mu\text{-O})\text{Fe}]^{3+}$, and $[\text{Fe}(\text{OH})(\mu\text{-O})\text{Fe}(\text{OH})]^{3+}$ with formal oxidation states of ($\mu\text{-oxo}$)diiron(II,III), ($\mu\text{-oxo}$)diiron(III), and ($\mu\text{-oxo}$)diiron(III,IV), respectively. Each of the aforementioned iron-oxo species were already discussed in the context of the proposed mechanisms shown in Scheme 1 and Scheme 2 with the exception of $[\text{Fe}(\text{OH})(\mu\text{-O})\text{Fe}(\text{OH})]^{3+}$; stoichiometrically, this active site motif would require two or more equivalents of H_2O_2 (for example) to generate adjacent terminal hydroxide ligands. The reactivity of $[\text{Fe}(\text{OH})(\mu\text{-O})\text{Fe}(\text{OH})]^{3+}$ is shown in Table S13, and it has a predicted methane activation barrier that is comparable to $[\text{Fe}(\text{O})]^{2+}$ at the PBE-D3(BJ)+*U* level of theory.

To better understand the electronic structure, we computed the Charge Model 5 (CM5)^{72,73} partial atomic charges for each iron-oxo species (Figure 5). Since partial atomic charges are not numerically equivalent to oxidation states, we use the CM5 charges of the iron sites in guest-free $\text{Fe}_2(\mu\text{-OH})_2(\text{bbta})$ as a reference point for the 2+ oxidation state. The reference point for the 3+ oxidation state is obtained from CM5 charges of the metal centers if they were to all contain a terminal OH ligand (i.e. $\text{Fe}_2(\text{OH})_2(\mu\text{-OH})_2(\text{bbta})$).

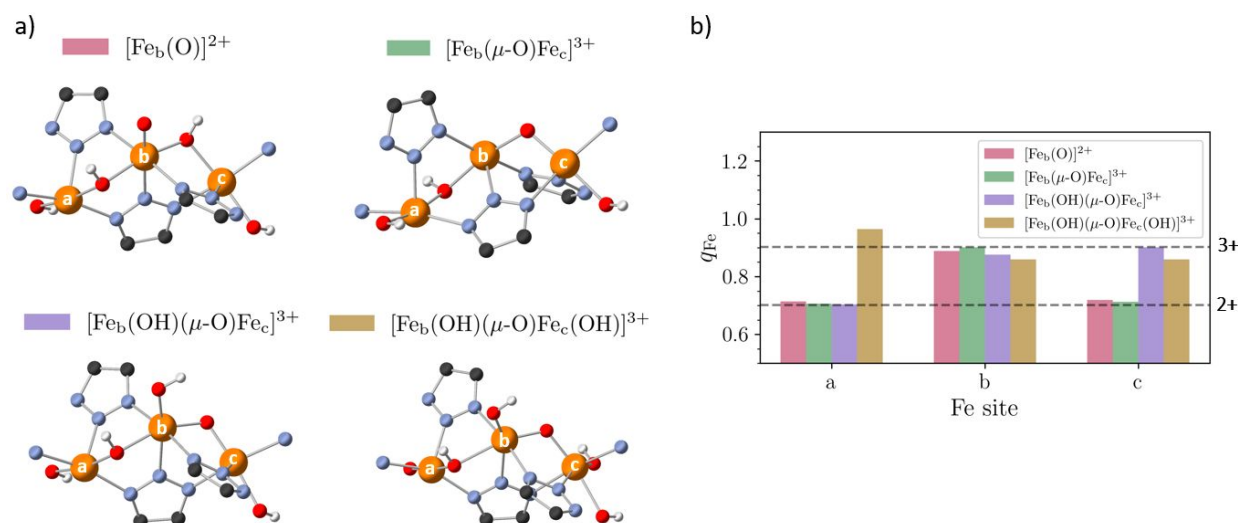


Figure 5. a) Representative portions of the DFT-optimized geometries of four different iron-oxo species with unique electronic structure environments. b) Charge Model 5 (CM5) partial atomic charges, q_{Fe} , at the iron (Fe) centers for each structure. The CM5 charges correspond to the metals “a”, “b”, and “c”, with the terminal oxo ligand found at metal “b” and the bridging oxo ligand between metals “b” and “c”. Reference CM5 values for the 2+ and 3+ oxidation states are shown as dashed, horizontal lines. Results are presented at the PBE-D3(BJ)+*U* level of theory. Color key: $[\text{Fe}_b(\text{O})]^{2+}$ (red), $[\text{Fe}_b(\mu\text{-O})\text{Fe}_c]^{3+}$ (green), $[\text{Fe}_b(\text{OH})(\mu\text{-O})\text{Fe}_c]^{3+}$ (purple), $[\text{Fe}_b(\text{OH})(\mu\text{-O})\text{Fe}_c(\text{OH})]^{3+}$ (brown). Atom color key: Fe (orange), O (red), N (blue), C (black), H (white).

As shown in Figure 5, the $[\text{Fe}_b(\text{O})]^{2+}$ site is best-described as having primarily Fe(III) character based on the CM5 partial charge analysis, compared with a formal oxidation state of 4+. For the $[\text{Fe}_b(\mu\text{-O})\text{Fe}_c]^{3+}$ species, the metal centers are not predicted to be electronically identical, and one of the metals exhibits more Fe(III) character than the other despite having the same coordination environment. In this case, the $[\text{Fe}_b(\mu\text{-O})\text{Fe}_c]^{3+}$ species is well-described by the formal oxidation state of diiron(II,III). The electronic structure of the $[\text{Fe}_b(\text{OH})(\mu\text{-O})\text{Fe}_c]^{3+}$ species is analogous to that of the $[\text{Fe}_b(\mu\text{-O})\text{Fe}_c]^{3+}$ species except that both metal centers are now oxidized according to the partial charge analysis, with the best description being a diiron(III) state (Figure 5). The $[\text{Fe}_b(\text{OH})(\mu\text{-O})\text{Fe}_c(\text{OH})]^{3+}$ species is more complex and exhibits intrachain charge transfer such that a metal center on the periphery of the $[\text{Fe}_b(\text{OH})(\mu\text{-O})\text{Fe}_c(\text{OH})]^{3+}$ species, denoted Fe_a , also gets oxidized. This behavior is qualitatively similar to that of $\text{Fe}_2(\text{dobdc})$, which reacts with O_2 at room temperature to form an iron-peroxo complex where one electron is believed to come from the iron binding site while the second electron comes from an adjacent iron atom.⁸⁴

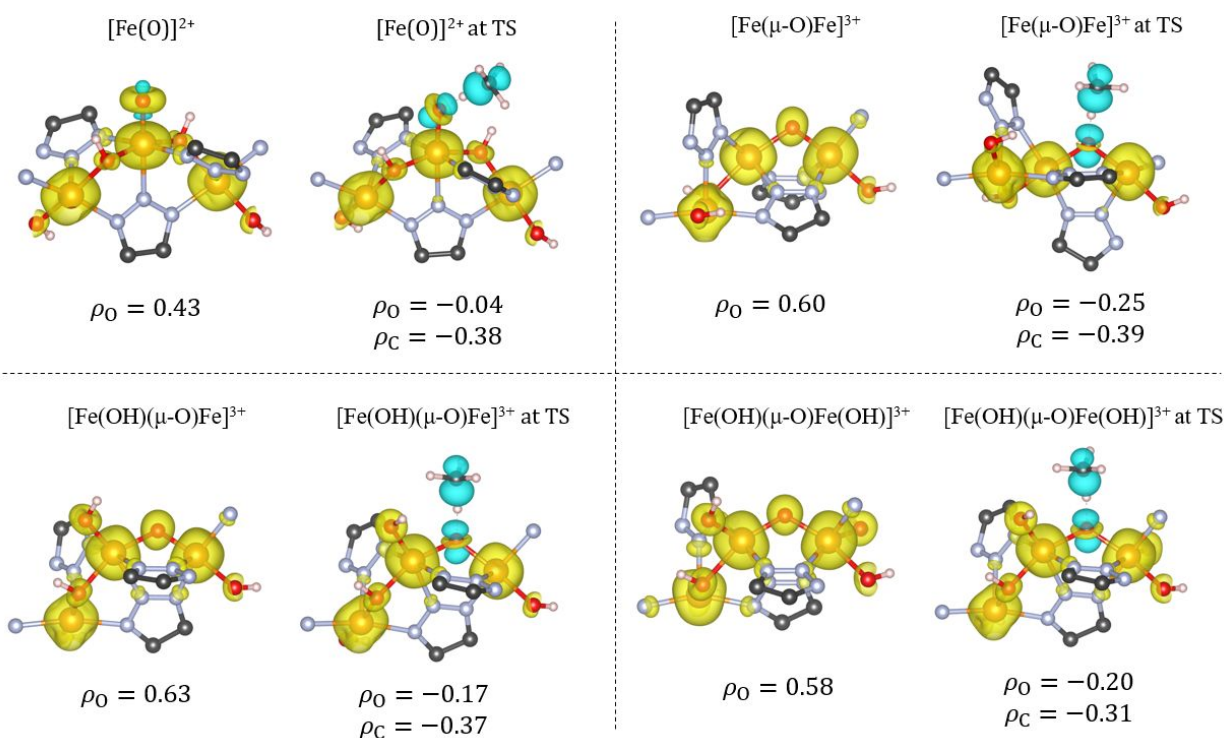


Figure 6. Spin densities for several iron-oxo species both before and at the transition state (TS) for C–H activation. The Bader atomic spin moment on the abstracting oxo ligand, ρ_O , and carbon atom of the methyl radical, ρ_C , are shown. Note that the spin density surface on the peripheral oxygen atoms is truncated due to periodic boundary conditions and that the viewing angles are slightly different for ease of visualization. Only representative portions of the DFT-optimized structures are shown. Spin density color key: positive spin density (yellow), negative spin density (cyan). Atom color key: Fe (orange), O (red), N (blue), C (black), H (white).

A complementary approach to investigate the electronic structure of these iron-oxo species is to analyze the spin density surfaces and atomic spin moments, as shown in Figure 6. Taking the spin density on the iron sites as positive by convention, the bridging oxo ligands exhibit a substantial degree of positive spin density prior to C–H activation (i.e. $\rho_O = 0.58 - 0.63$). Changes in the formal oxidation state of the iron centers do not appear to drastically alter the spin density of the bridging oxo ligand in this MOF. While the terminal oxo ligand has primarily positive spin density as well ($\rho_O = 0.43$), we note that there is a small but non-negligible amount of negative spin density localized on the oxygen atom. This mixture of spin density is arranged in a donut–dumbbell shape, where the donut (yellow) and dumbbell (cyan) are of opposite spin. An analogous type of donut–dumbbell mixed spin density profile has been predicted for at least one other terminal iron-oxo species in the literature, albeit for a completely different coordination environment based on tetracarbene ligands.⁸⁵

At the transition state for C–H activation, all the investigated oxo ligands exhibit a mixture of positive and negative spin density, although it is the most pronounced for the terminal oxo ligand. In the case of the $[\text{Fe}(\text{O})]^{2+}$ species, the donut–dumbbell shape is still present at the transition state, although the signs of the majority and minority spin densities have reversed. The transition from a positive to negative net effective spin moment on the terminal oxo ligand has been noted in prior work on Mg-diluted $\text{Fe}_2(\mu\text{-OH})_2(\text{bbta})^{23}$ as well as other $[\text{Fe}(\text{O})]^{2+}$ sites in the literature⁸⁶ and can significantly reduce the activation energy for H-abstraction, likely due to exchange-enhancement.⁸⁷

Since the opposite-sign spin densities shown in Figure 6 reduce the net atomic spin moment, this suggests that the “degree of radical character” on the oxo/oxy ligand may not always be well-represented by a typical population analysis. The mixing of opposite-sign spin densities on the abstracting atom may be one of several factors that occasionally prevents a direct relationship to be drawn between the atomic spin moment and the catalytic reactivity.^{23,88} Given the demonstrated utility of rationalizing H-abstraction reactions in the context of spin density on the abstracting atom,^{89–91} it may be more predictive to consider the orbital-specific radical character as opposed to the net atomic spin moment, although this can be more difficult to systematically quantify with DFT.

Conclusions

In this work, we computationally investigated the formation and subsequent reactivity of terminal iron-oxo sites and bridging iron-oxo sites in $\text{Fe}_2(\mu\text{-OH})_2(\text{bbta})$, specifically focusing on the direct conversion of methane to methanol as a test of its ability to activate strong C–H bonds. When considering N_2O as a potential oxidant, $\text{Fe}_2(\mu\text{-OH})_2(\text{bbta})$ exhibits a relatively low barrier for N_2O activation while having an exothermic reaction energy for $[\text{Fe}(\text{O})]^{2+}$ formation. We also predict that the incorporation of $\mu\text{-OH}^-$ ligands – as opposed to $\mu\text{-Cl}^-$ ligands in the parent $\text{Fe}_2(\mu\text{-Cl})_2(\text{bbta})$ framework – is especially beneficial for the N_2O activation process. When considering an oxidant that generates $\text{OH}\cdot$ radicals, such as H_2O_2 , the mechanistic complexity is far greater, and numerous types of iron-oxo sites can potentially be realized, including $[\text{Fe}(\text{O})]^{2+}$ sites and bridging iron-oxo species of various formal oxidation states (e.g. $[\text{Fe}(\mu\text{-O})\text{Fe}]^{3+}$ vs. $[\text{Fe}(\text{OH})(\mu\text{-O})\text{Fe}]^{3+}$ vs. $[\text{Fe}(\text{OH})(\mu\text{-O})\text{Fe}(\text{OH})]^{3+}$). The $[\text{Fe}(\text{O})]^{2+}$ species is predicted to be more reactive towards strong C–H bonds than most of the bridging iron-oxo sites studied in this work, although it is more likely to form with N_2O than H_2O_2 . When investigating the spin density surfaces, we find that a complex mixture of positive and negative spin density can simultaneously reside on the oxo ligand, particularly for the $[\text{Fe}(\text{O})]^{2+}$ species and at the transition states for C–H activation.

Motivated by the mechanistic analyses presented in this work, there are several factors not explored here that would be worth considering in future work. For instance, the use of post-synthesis metal-exchange to yield a mixed-metal framework may make it possible to further tune the reactive properties of the $\text{M}_2(\mu\text{-OH})_2(\text{bbta})$ MOF family. As one example, doping a framework that cannot be readily oxidized, such as a hypothetical $\text{Cu}_2(\mu\text{-OH})_2(\text{bbta})$ framework, with spatially isolated Fe sites may decrease the likelihood of forming bridging iron-oxo species in favor of terminal oxo ligands at the redox-active metal centers. The use of a redox-inactive host framework may also increase the stability of the proposed catalyst since it is known that the structurally related $\text{Fe}_2(\mu\text{-Cl})_2(\text{btdd})$ framework is irreversibly oxidized when exposed to air.⁹² Beyond this specific MOF family, the feasibility of forming $[\text{FeO}]^{2+}$ in $\text{Fe}_2(\mu\text{-OH})_2(\text{bbta})$ suggests that it may be worthwhile to explore the possibility of forming terminal oxo species as reactive intermediates in Fe-exchanged MFU-4l (MFU = Metal–Organic Framework Ulm),⁹³ which is a cubic analogue of the hexagonal, large-pore $\text{M}_2(\mu\text{-OH})_2(\text{btdd})$ framework but with mononuclear Fe(II) sites. Finally, we acknowledge that mechanistic pathways beyond those directly investigated in this work are necessary to better understand questions about the selectivity towards various products,^{35,40} and other reaction intermediates can undoubtedly be considered.

Collectively, the density functional theory calculations in this work provide support for the hypothesis that Fe sites incorporated within the $\text{M}_2(\mu\text{-OH})_2(\text{bbta})$ family of metal–triazolate frameworks may be able to form iron-oxo species capable of activating C–H bonds. Based on a comparison of the mechanistic pathways involving N_2O and H_2O_2 oxidants, we would recommend the use of N_2O since it is more likely to result in the formation of Fe(IV)-oxo intermediates, which are predicted to be more reactive towards C–H bonds than the various bridging iron-oxo sites that may form in the presence of H_2O_2 . More generally, the highly tunable nature of this MOF family combined with the redox activity of the Fe(II) sites

suggest that this and related metal–triazolate frameworks may be worth considering for catalytic oxidation reactions, especially if the goal is to gain a better understanding of fundamental structure–property relationships.

Conflicts of Interest

There are no conflicts to declare.

Acknowledgments

A.S.R.: conceptualization, data curation, formal analysis, funding acquisition, investigation, methodology, resources, software, validation, visualization, writing – original draft, writing – reviewing and editing; J.M.N.: project administration, supervision; R.Q.S.: project administration, supervision.

Acknowledgments

A.S.R. was supported by a fellowship award through the National Defense Science and Engineering Graduate (NDSEG) Fellowship Program, sponsored by the Air Force Research Laboratory (AFRL), the Office of Naval Research (ONR) and the Army Research Office (ARO). A.S.R. also acknowledges support from a Ryan Fellowship through the International Institute for Nanotechnology as well a Presidential Fellowship through The Graduate School at Northwestern University. The material in this work is supported by the Institute for Catalysis in Energy Processes (ICEP) via the U.S. Department of Energy, Office of Science, Office of Basic Energy Sciences (award number DE-FG02-03ER15457). The authors acknowledge computing support from the Quest high-performance computing facility at Northwestern University.

References

- (1) Gunay, A.; Theopold, K. H. C–H Bond Activations by Metal Oxo Compounds. *Chem. Rev.* **2010**, *110* (2), 1060–1081.
- (2) Larson, V. A.; Battistella, B.; Ray, K.; Lehnert, N.; Nam, W. Iron and Manganese Oxo Complexes, Oxo Wall and Beyond. *Nat. Rev. Chem.* **2020**, *4* (8), 404–419.
- (3) Hohenberger, J.; Ray, K.; Meyer, K. The Biology and Chemistry of High-Valent Iron–Oxo and Iron–Nitrido Complexes. *Nat. Commun.* **2012**, *3* (1), 720.
- (4) Ray, K.; Pfaff, F. F.; Wang, B.; Nam, W. Status of Reactive Non-Heme Metal–Oxygen Intermediates in Chemical and Enzymatic Reactions. *J. Am. Chem. Soc.* **2014**, *136* (40), 13942–13958.
- (5) Chen, Z.; Yin, G. The Reactivity of the Active Metal Oxo and Hydroxo Intermediates and Their Implications in Oxidations. *Chem. Soc. Rev.* **2015**, *44* (5), 1083–1100.
- (6) Engelmann, X.; Monte-Pérez, I.; Ray, K. Oxidation Reactions with Bioinspired Mononuclear Non-Heme Metal–Oxo Complexes. *Angew. Chemie Int. Ed.* **2016**, *55* (27), 7632–7649.
- (7) Shimoyama, Y.; Kojima, T. Metal–Oxyl Species and Their Possible Roles in Chemical Oxidations. *Inorg. Chem.* **2019**, *58* (15), 9517–9542.
- (8) Guo, M.; Corona, T.; Ray, K.; Nam, W. Heme and Nonheme High-Valent Iron and Manganese Oxo Cores in Biological and Abiological Oxidation Reactions. *ACS Cent. Sci.* **2019**, *5* (1), 13–28.
- (9) Jiao, L.; Wang, Y.; Jiang, H.; Xu, Q. Metal–Organic Frameworks as Platforms for Catalytic Applications. *Adv. Mater.* **2017**, *30* (37), 1703663.

- (10) Wasson, M. C.; Buru, C. T.; Chen, Z.; Islamoglu, T.; Farha, O. K. Metal–Organic Frameworks: A Tunable Platform to Access Single-Site Heterogeneous Catalysts. *Appl. Catal. A Gen.* **2019**, 117214.
- (11) Wang, C.; An, B.; Lin, W. Metal–Organic Frameworks in Solid–Gas Phase Catalysis. *ACS Catal.* **2019**, *9* (1), 130–146.
- (12) Yang, D.; Gates, B. C. Catalysis by Metal Organic Frameworks: Perspective and Suggestions for Future Research. *ACS Catal.* **2019**, *9* (3), 1779–1798.
- (13) Sun, C.; Yang, L.; Ortuño, M. A.; Wright, A. M.; Chen, T.; Head, A. R.; López, N.; Dincă, M. Spectroscopic Evidence of Hyponitrite Radical Intermediate in NO Disproportionation at a MOF-Supported Mononuclear Copper Site. *Angew. Chemie Int. Ed.* **2021**, *60* (14), 7845–7850.
- (14) Liu, M.; Wu, J.; Hou, H. Metal–Organic Frameworks Based Materials as Heterogeneous Catalysts for C–H Bond Activation. *Chem. – A Eur. J.* **2018**, *25* (12), 2935–2948.
- (15) Hall, J. N.; Li, M.; Bollini, P. Light Alkane Oxidation over Well-Defined Active Sites in Metal–Organic Framework Materials. *Catal. Sci. Technol.* **2022**.
- (16) Xiao, D. J.; Bloch, E. D.; Mason, J. A.; Queen, W. L.; Hudson, M. R.; Planas, N.; Borycz, J.; Dzubak, A. L.; Verma, P.; Lee, K.; Bonino, F.; Crocellà, V.; Yano, J.; Bordiga, S.; Truhlar, D. G.; Gagliardi, L.; Brown, C. M.; Long, J. R. Oxidation of Ethane to Ethanol by N₂O in a Metal–Organic Framework with Coordinatively Unsaturated Iron(II) Sites. *Nat. Chem.* **2014**, *6* (7), 590–595.
- (17) Verma, P.; Vogiatzis, K. D.; Planas, N.; Borycz, J.; Xiao, D. J.; Long, J. R.; Gagliardi, L.; Truhlar, D. G. Mechanism of Oxidation of Ethane to Ethanol at Iron(IV)-Oxo Sites in Magnesium-Diluted Fe₂(DOBDC). *J. Am. Chem. Soc.* **2015**, *137* (17), 5770–5781.
- (18) Hirao, H.; Ng, W. K. H.; Moeljadi, A. M. P.; Bureekaew, S. Multiscale Model for a Metal–Organic Framework: High-Spin Rebound Mechanism in the Reaction of the Oxoiron(IV) Species of Fe-MOF-74. *ACS Catal.* **2015**, *5* (6), 3287–3291.
- (19) Saiz, F.; Bernasconi, L. Electronic Structure and Reactivity of Fe(IV) Oxo Species in Metal–Organic Frameworks. *Phys. Chem. Chem. Phys.* **2019**, *21* (9), 4965–4974.
- (20) Saiz, F.; Bernasconi, L. Density-Functional Theory Models of Fe(IV)O Reactivity in Metal–Organic Frameworks: Self-Interaction Error, Spin Delocalisation and the Role of Hybrid Exchange. *Phys. Chem. Chem. Phys.* **2020**, *22* (22), 12821–12830.
- (21) Hall, J. N.; Bollini, P. Low-Temperature, Ambient Pressure Oxidation of Methane to Methanol Over Every Tri-Iron Node in a Metal–Organic Framework Material. *Chem. Eur. J.* **2020**, *26* (70), 16639–16643.
- (22) Barona, M.; Ahn, S.; Morris, W.; Hoover, W. J.; Notestein, J. M.; Farha, O. K.; Snurr, R. Q. Computational Predictions and Experimental Validation of Alkane Oxidative Dehydrogenation by Fe₂M MOF Nodes. *ACS Catal.* **2020**, *10* (2), 1460–1469.
- (23) Rosen, A. S.; Notestein, J. M.; Snurr, R. Q. High-Valent Metal-Oxo Species at the Nodes of Metal–Triazolate Frameworks: The Effects of Ligand-Exchange and Two-State Reactivity for C–H Bond Activation. *Angew. Chemie Int. Ed.* **2020**, *132* (44), 19662–19670.
- (24) Rosen, A. S.; Notestein, J. M.; Snurr, R. Q. Structure–Activity Relationships That Identify Metal–Organic Framework Catalysts for Methane Activation. *ACS Catal.* **2019**, *9*, 3576–3587.
- (25) Hall, J.; Bollini, P. Role of Metal Identity and Speciation in the Low-Temperature Oxidation of Methane over Tri-Metal Oxo Clusters. *Authorea* **2021**.

<https://doi.org/10.22541/au.162027355.57700091/v1>.

- (26) Rosen, A. S.; Notestein, J. M.; Snurr, R. Q. Identifying Promising Metal–Organic Frameworks for Heterogeneous Catalysis via High-Throughput Periodic Density Functional Theory. *J. Comput. Chem.* **2019**, *40* (12), 1305–1318.
- (27) Simons, M. C.; Vitillo, J. G.; Babucci, M.; Hoffman, A. S.; Boubnov, A.; Beauvais, M. L.; Chen, Z.; Cramer, C. J.; Chapman, K. W.; Bare, S. R.; Gates, B. C.; Lu, C. C.; Gagliardi, L.; Bhan, A. Structure, Dynamics, and Reactivity for Light Alkane Oxidation of Fe(II) Sites Situated in the Nodes of a Metal–Organic Framework. *J. Am. Chem. Soc.* **2019**, *141* (45), 18142–18151.
- (28) Vitillo, J. G.; Bhan, A.; Cramer, C. J.; Lu, C. C.; Gagliardi, L. Quantum Chemical Characterization of Structural Single Fe(II) Sites in MIL-Type Metal Organic Frameworks for Oxidation of Methane to Methanol and Ethane to Ethanol. *ACS Catal.* **2019**, *9*, 2870–2879.
- (29) Barona, M.; Snurr, R. Q. Exploring the Tunability of Trimetallic MOF Nodes for Partial Oxidation of Methane to Methanol. *ACS Appl. Mater. Interfaces* **2020**, *12* (25), 28217–28231.
- (30) Vitillo, J. G.; Lu, C. C.; Cramer, C. J.; Bhan, A.; Gagliardi, L. Influence of First and Second Coordination Environment on Structural Fe(II) Sites in MIL-101 for C–H Bond Activation in Methane. *ACS Catal.* **2020**, *11*, 579–589.
- (31) Vogiatzis, K. D.; Haldoupis, E.; Xiao, D. J.; Long, J. R.; Siepmann, J. I.; Gagliardi, L. Accelerated Computational Analysis of Metal–Organic Frameworks for Oxidation Catalysis. *J. Phys. Chem. C* **2016**, *120* (33), 18707–18712.
- (32) Impeng, S.; Siwaipram, S.; Bureekaew, S.; Probst, M. Ethane C–H Bond Activation on the Fe(IV)–Oxo Species in a Zn-Based Cluster of Metal–Organic Frameworks: A Density Functional Theory Study. *Phys. Chem. Chem. Phys.* **2017**, *19* (5), 3782–3791.
- (33) Suh, B. L.; Kim, J. Ligand Insertion in MOF-74 as Effective Design for Oxidation of Ethane to Ethanol. *J. Phys. Chem. C* **2018**, *122* (40), 23078–23083.
- (34) Zhao, W.; Shi, Y.; Jiang, Y.; Zhang, X.; Long, C.; An, P.; Zhu, Y.; Shao, S.; Yan, Z.; Li, G.; Tang, Z. Fe–O Clusters Anchored on Nodes of Metal–Organic Frameworks for Direct Methane Oxidation. *Angew. Chemie Int. Ed.* **2020**, *60* (11), 5811–5815.
- (35) Simons, M. C.; Prinslow, S. D.; Babucci, M.; Hoffman, A. S.; Hong, J.; Vitillo, J. G.; Bare, S. R.; Gates, B. C.; Lu, C. C.; Gagliardi, L.; Bhan, A. Beyond Radical Rebound: Methane Oxidation to Methanol Catalyzed by Iron Species in Metal–Organic Framework Nodes. *J. Am. Chem. Soc.* **2021**, *143* (31), 12165–12174.
- (36) Pahls, D. R.; Ortuño, M. A.; Winegar, P. H.; Cramer, C. J.; Gagliardi, L. Computational Screening of Bimetal-Functionalized Zr₆O₈ MOF Nodes for Methane C–H Bond Activation. *Inorg. Chem.* **2017**, *56* (15), 8739–8743.
- (37) Ikuno, T.; Zheng, J.; Vjunov, A.; Sanchez-Sanchez, M.; Ortuño, M. A.; Pahls, D. R.; Fulton, J. L.; Camaioni, D. M.; Li, Z.; Ray, D.; Mehdi, B. L.; Browning, N. D.; Farha, O. K.; Hupp, J. T.; Cramer, C. J.; Gagliardi, L.; Lercher, J. A. Methane Oxidation to Methanol Catalyzed by Cu–Oxo Clusters Stabilized in NU-1000 Metal–Organic Framework. *J. Am. Chem. Soc.* **2017**, *139* (30), 10294–10301.
- (38) Baek, J.; Rungtaweeworanit, B.; Pei, X.; Park, M.; Fakra, S. C.; Liu, Y.-S.; Matheu, R.; Alshimiri, S. A.; Alshihri, S.; Trickett, C. A.; Somorjai, G. A.; Yaghi, O. M. Bioinspired Metal–Organic Framework Catalysts for Selective Methane Oxidation to Methanol. *J. Am. Chem. Soc.* **2018**, *140* (51), 18208–18216.

- (39) Osadchii, D.; Olivos Suarez, A. I.; Szécsényi, Á.; Li, G.; Nasalevich, M. A.; Dugulan, A. I.; Serra-Crespo, P.; Hensen, E. J. M.; Veber, S. L.; Fedin, M. V.; Sankar, G.; Pidko, E. A.; Gascon, J. Isolated Fe Sites in Metal–Organic Framework Catalyze the Direct Conversion of Methane to Methanol. *ACS Catal.* **2018**, *8* (6), 5542–5548.
- (40) Szécsényi, Á.; Li, G.; Gascon, J.; Pidko, E. A. Unraveling Reaction Networks behind the Catalytic Oxidation of Methane with H₂O₂ over a Mixed-Metal MIL-53(Al,Fe) MOF Catalyst. *Chem. Sci.* **2018**, *9* (33), 6765–6773.
- (41) Liao, P.-Q.; Li, X.-Y.; Bai, J.; He, C.-T.; Zhou, D.-D.; Zhang, W.-X.; Zhang, J.-P.; Chen, X.-M. Drastic Enhancement of Catalytic Activity via Post-Oxidation of a Porous Mn^{II} Triazolate Framework. *Chem. Eur. J.* **2014**, *20* (36), 11303–11307.
- (42) Reed, D. A.; Keitz, B. K.; Oktawiec, J.; Mason, J. A.; Runčevski, T.; Xiao, D. J.; Darago, L. E.; Crocellà, V.; Bordiga, S.; Long, J. R. A Spin Transition Mechanism for Cooperative Adsorption in Metal–Organic Frameworks. *Nature* **2017**, *550* (7674), 96–100.
- (43) Liao, P.-Q.; Chen, H.; Zhou, D.-D.; Liu, S.-Y.; He, C.-T.; Rui, Z.; Ji, H.; Zhang, J.-P.; Chen, X.-M. Monodentate Hydroxide as a Super Strong yet Reversible Active Site for CO₂ Capture from High-Humidity Flue Gas. *Energy Environ. Sci.* **2015**, *8* (3), 1011–1016.
- (44) Rieth, A. J.; Wright, A. M.; Rao, S.; Kim, H.; LaPotin, A. D.; Wang, E. N.; Dincă, M. Tunable Metal–Organic Frameworks Enable High-Efficiency Cascaded Adsorption Heat Pumps. *J. Am. Chem. Soc.* **2018**, *140* (50), 17591–17596.
- (45) Huang, N.-Y.; He, H.; Li, H.; Liao, P.-Q.; Chen, X.-M. A Metal–Organic Framework with in Situ Generated Low-Coordinate Binuclear Cu(I) Units as a Highly Effective Catalyst for Photodriven Hydrogen Production. *Chem. Commun.* **2020**, *56* (49), 6700–6703.
- (46) Rieth, A. J.; Tulchinsky, Y.; Dincă, M. High and Reversible Ammonia Uptake in Mesoporous Azolate Metal–Organic Frameworks with Open Mn, Co, and Ni Sites. *J. Am. Chem. Soc.* **2016**, *138* (30), 9401–9404.
- (47) Tulchinsky, Y.; Hendon, C. H.; Lomachenko, K. A.; Borfecchia, E.; Melot, B. C.; Hudson, M. R.; Tarver, J. D.; Korzyński, M. D.; Stubbs, A. W.; Kagan, J. J.; Lamberti, C.; Brown, C. M.; Dincă, M. Reversible Capture and Release of Cl₂ and Br₂ with a Redox-Active Metal–Organic Framework. *J. Am. Chem. Soc.* **2017**, *139* (16), 5992–5997.
- (48) Rosen, A. S.; Mian, M. R.; Islamoglu, T.; Chen, H.; Farha, O. K.; Notestein, J. M.; Snurr, R. Q. Tuning the Redox Activity of Metal–Organic Frameworks for Enhanced, Selective O₂ Binding: Design Rules and Ambient Temperature O₂ Chemisorption in a Cobalt–Triazolate Framework. *J. Am. Chem. Soc.* **2020**, *142* (9), 4317–4328.
- (49) Rosen, A. S.; Notestein, J. M.; Snurr, R. Q. Comparing GGA, GGA+U, and Meta-GGA Functionals for Redox-Dependent Binding at Open Metal Sites in Metal–Organic Frameworks. *J. Chem. Phys.* **2020**, *152*, 224101.
- (50) Oktawiec, J.; Jiang, H. Z. H.; Vitillo, J. G.; Reed, D. A.; Darago, L. E.; Trump, B. A.; Bernales, V.; Li, H.; Colwell, K. A.; Furukawa, H.; Brown, C. M.; Gagliardi, L.; Long, J. R. Negative Cooperativity upon Hydrogen Bond-Stabilized O₂ Adsorption in a Redox-Active Metal–Organic Framework. *Nat. Commun.* **2020**, *11*, 3087.
- (51) Ravi, M.; Ranocchiari, M.; van Bokhoven, J. A. The Direct Catalytic Oxidation of Methane to Methanol — A Critical Assessment. *Angew. Chemie Int. Ed.* **2017**, *56* (52), 16464–16483.
- (52) Zichittella, G.; Pérez-Ramírez, J. Status and Prospects of the Decentralised Valorisation of Natural

- Gas into Energy and Energy Carriers. *Chem. Soc. Rev.* **2021**, *50* (5), 2984–3012.
- (53) Dinh, K. T.; Sullivan, M. M.; Serna, P.; Meyer, R. J.; Dincă, M.; Román-Leshkov, Y. Viewpoint on the Partial Oxidation of Methane to Methanol Using Cu- and Fe-Exchanged Zeolites. *ACS Catal.* **2018**, *8* (9), 8306–8313.
- (54) Lu, X.-F.; Liao, P.-Q.; Wang, J.-W.; Wu, J.-X.; Chen, X.-W.; He, C.-T.; Zhang, J.-P.; Li, G.-R.; Chen, X.-M. An Alkaline-Stable, Metal Hydroxide Mimicking Metal–Organic Framework for Efficient Electrocatalytic Oxygen Evolution. *J. Am. Chem. Soc.* **2016**, *138* (27), 8336–8339.
- (55) Wang, Y.; Huang, N.-Y.; Shen, J.-Q.; Liao, P.-Q.; Chen, X.-M.; Zhang, J.-P. Hydroxide Ligands Cooperate with Catalytic Centers in Metal–Organic Frameworks for Efficient Photocatalytic CO₂ Reduction. *J. Am. Chem. Soc.* **2018**, *140* (1), 38–41.
- (56) Kresse, G.; Furthmüller, J. Efficient Iterative Schemes for Ab Initio Total-Energy Calculations Using a Plane-Wave Basis Set. *Phys. Rev. B* **1996**, *54* (16), 11169–11186.
- (57) Kresse, G.; Joubert, D. From Ultrasoft Pseudopotentials to the Projector Augmented-Wave Method. *Phys. Rev. B* **1999**, *59* (3), 1758–1775.
- (58) Bernales, V.; Ortuño, M. A.; Truhlar, D. G.; Cramer, C. J.; Gagliardi, L. Computational Design of Functionalized Metal–Organic Framework Nodes for Catalysis. *ACS Cent. Sci.* **2018**, *4* (1), 5–19.
- (59) Perdew, J. P.; Burke, K.; Ernzerhof, M. Generalized Gradient Approximation Made Simple. *Phys. Rev. Lett.* **1996**, *77* (18), 3865–3868.
- (60) Grimme, S.; Antony, J.; Ehrlich, S.; Krieg, H. A Consistent and Accurate Ab Initio Parametrization of Density Functional Dispersion Correction (DFT-D) for the 94 Elements H–Pu. *J. Chem. Phys.* **2010**, *132* (15), 154104.
- (61) Grimme, S.; Ehrlich, S.; Goerigk, L. Effect of the Damping Function in Dispersion Corrected Density Functional Theory. *J. Comput. Chem.* **2011**, *32* (7), 1456–1465.
- (62) Dudarev, S. L.; Botton, G. A.; Savrasov, S. Y.; Humphreys, C. J.; Sutton, A. P. Electron-Energy-Loss Spectra and the Structural Stability of Nickel Oxide: An LSDA+U Study. *Phys. Rev. B* **1998**, *57* (3), 1505.
- (63) Wang, L.; Maxisch, T.; Ceder, G. Oxidation Energies of Transition Metal Oxides within the GGA+U Framework. *Phys. Rev. B* **2006**, *73* (19), 195107.
- (64) Lee, K.; Howe, J. D.; Lin, L.-C.; Smit, B.; Neaton, J. B. Small-Molecule Adsorption in Open-Site Metal–Organic Frameworks: A Systematic Density Functional Theory Study for Rational Design. *Chem. Mater.* **2015**, *27* (3), 668–678.
- (65) Vlaisavljevich, B.; Huck, J.; Hulvey, Z.; Lee, K.; Mason, J. A.; Neaton, J. B.; Long, J. R.; Brown, C. M.; Alfè, D.; Michaelides, A.; Smit, B. Performance of van Der Waals Corrected Functionals for Guest Adsorption in the M₂(DOBDC) Metal–Organic Frameworks. *J. Phys. Chem. A* **2017**, *121* (21), 4139–4151.
- (66) Kulik, H. J. Perspective: Treating Electron Over-Delocalization with the DFT+U Method. *J. Chem. Phys.* **2015**, *142* (24), 240901.
- (67) Monkhorst, H. J.; Pack, J. D. Special Points for Brillouin-Zone Integrations. *Phys. Rev. B* **1976**, *13* (12), 5188–5192.
- (68) Borycz, J.; Paier, J.; Verma, P.; Darago, L. E.; Xiao, D. J.; Truhlar, D. G.; Long, J. R.; Gagliardi, L. Structural and Electronic Effects on the Properties of Fe₂(Dobdc) upon Oxidation with N₂O. *Inorg.*

- Chem.* **2016**, *55* (10), 4924–4934.
- (69) Henkelman, G.; Uberuaga, B. P.; Jónsson, H. A Climbing Image Nudged Elastic Band Method for Finding Saddle Points and Minimum Energy Paths. *J. Chem. Phys.* **2000**, *113* (22), 9901–9904.
- (70) Henkelman, G.; Jónsson, H. A Dimer Method for Finding Saddle Points on High Dimensional Potential Surfaces Using Only First Derivatives. *J. Chem. Phys.* **1999**, *111* (15), 7010–7022.
- (71) Henkelman, G. VTST Tools <http://theory.cm.utexas.edu/vtsttools/index.html>.
- (72) Marenich, A. V.; Jerome, S. V.; Cramer, C. J.; Truhlar, D. G. Charge Model 5: An Extension of Hirshfeld Population Analysis for the Accurate Description of Molecular Interactions in Gaseous and Condensed Phases. *J. Chem. Theory Comput.* **2012**, *8* (2), 527–541.
- (73) Manz, T. A.; Gabaldon Limas, N. Chargemol program for performing DDEC analysis <http://ddec.sourceforge.net/>.
- (74) Tang, W.; Sanville, E.; Henkelman, G. A Grid-Based Bader Analysis Algorithm without Lattice Bias. *J. Phys. Condens. Matter* **2009**, *21* (8), 84204.
- (75) Wang, V.; Xu, N.; Liu, J.-C.; Tang, G.; Geng, W.-T. VASPKIT: A User-Friendly Interface Facilitating High-Throughput Computing and Analysis Using VASP Code. *Comput. Phys. Commun.* **2021**, *267*, 108033.
- (76) Momma, K.; Izumi, F. VESTA 3 for Three-Dimensional Visualization of Crystal, Volumetric and Morphology Data. *J. Appl. Crystallogr.* **2011**, *44* (6), 1272–1276.
- (77) Capdevila-Cortada, M.; Łodziana, Z.; López, N. Performance of DFT+U Approaches in the Study of Catalytic Materials. *ACS Catal.* **2016**, *6* (12), 8370–8379.
- (78) Heyd, J.; Scuseria, G. E.; Ernzerhof, M. Hybrid Functionals Based on a Screened Coulomb Potential. *J. Chem. Phys.* **2003**, *118* (18), 8207–8215.
- (79) Furche, F.; Perdew, J. P. The Performance of Semilocal and Hybrid Density Functionals in 3d Transition-Metal Chemistry. *J. Chem. Phys.* **2006**, *124* (4), 044103.
- (80) Moellmann, J.; Grimme, S. DFT-D3 Study of Some Molecular Crystals. *J. Phys. Chem. C* **2014**, *118* (14), 7615–7621.
- (81) Vennelakanti, V.; Nandy, A.; Kulik, H. The Effect of Hartree-Fock Exchange on Scaling Relations and Reaction Energetics for C–H Activation Catalysts. *Top. Catal.* **2021**.
- (82) Xiao, D. J.; Oktawiec, J.; Milner, P. J.; Long, J. R. Pore Environment Effects on Catalytic Cyclohexane Oxidation in Expanded Fe₂(Dobdc) Analogues. *J. Am. Chem. Soc.* **2016**, *138* (43), 14371–14379.
- (83) Latimer, A. A.; Aljama, H.; Kakekhani, A.; Yoo, J. S.; Kulkarni, A.; Tsai, C.; Garcia-Melchor, M.; Abild-Pedersen, F.; Nørskov, J. K. Mechanistic Insights into Heterogeneous Methane Activation. *Phys. Chem. Chem. Phys.* **2017**, *19* (5), 3575–3581.
- (84) Bloch, E. D.; Murray, L. J.; Queen, W. L.; Chavan, S.; Maximoff, S. N.; Bigi, J. P.; Krishna, R.; Peterson, V. K.; Grandjean, F.; Long, G. J.; Smit, B.; Bordiga, S.; Brown, C. M.; Long, J. R. Selective Binding of O₂ over N₂ in a Redox-Active Metal–Organic Framework with Open Iron(II) Coordination Sites. *J. Am. Chem. Soc.* **2011**, *133* (37), 14814–14822.
- (85) Kupper, C.; Mondal, B.; Serrano-Plana, J.; Klawitter, I.; Neese, F.; Costas, M.; Ye, S.; Meyer, F. Nonclassical Single-State Reactivity of an Oxo-Iron(IV) Complex Confined to Triplet Pathways. *J.*

- Am. Chem. Soc.* **2017**, *139* (26), 8939–8949.
- (86) Ye, S.; Neese, F. Nonheme Oxo-Iron(IV) Intermediates Form an Oxyl Radical upon Approaching the C–H Bond Activation Transition State. *Proc. Natl. Acad. Sci.* **2011**, *108* (4), 1228–1233.
- (87) Shaik, S.; Chen, H.; Janardanan, D. Exchange-Enhanced Reactivity in Bond Activation by Metal–Oxo Enzymes and Synthetic Reagents. *Nat. Chem.* **2011**, *3* (1), 19–27.
- (88) Liu, C.; Li, G.; Pidko, E. A. Property–Activity Relations for Methane Activation by Dual-Metal Cu–Oxo Trimers in ZSM-5 Zeolite. *Small Methods* **2018**, *2* (12), 1800266.
- (89) Dietl, N.; Schlangen, M.; Schwarz, H. Thermal Hydrogen-Atom Transfer from Methane: The Role of Radicals and Spin States in Oxo-Cluster Chemistry. *Angew. Chemie Int. Ed.* **2012**, *51* (23), 5544–5555.
- (90) Lai, W.; Li, C.; Chen, H.; Shaik, S. Hydrogen-Abstraction Reactivity Patterns from A to Y: The Valence Bond Way. *Angew. Chemie Int. Ed.* **2012**, *51* (23), 5556–5578.
- (91) Schwarz, H. Thermal Hydrogen-Atom Transfer from Methane: A Mechanistic Exercise. *Chem. Phys. Lett.* **2015**, *629*, 91–101.
- (92) Sun, L.; Hendon, C. H.; Park, S. S.; Tulchinsky, Y.; Wan, R.; Wang, F.; Walsh, A.; Dincă, M. Is Iron Unique in Promoting Electrical Conductivity in MOFs? *Chem. Sci.* **2017**, *8* (6), 4450–4457.
- (93) Denysenko, D.; Jelic, J.; Reuter, K.; Volkmer, D. Postsynthetic Metal and Ligand Exchange in MFU-4l: A Screening Approach toward Functional Metal–Organic Frameworks Comprising Single-Site Active Centers. *Chem. - A Eur. J.* **2015**, *21* (22), 8188–8199.